Time-resolved measurements of laser-induced shock waves in deuterated polystyrene porous targets by x-ray backlighting

R. Kodama, K. A. Tanaka, M. Nakai, K. Nishihara, T. Norimatsu, T. Yamanaka, and S. Nakai
Institute of Laser Engineering, Osaka University, Yamada-Oka 2-6, Suita, Osaka, 565 Japan

(Received 20 June 1989; accepted 12 September 1990)

Experimental studies are presented of laser-driven shock waves in deuterated polystyrene porous targets observed with x-ray streak shadowgraphy. Using two different target-mass densities of 0.1 g/cm^3 and 0.2 g/cm^3, the density dependence of the shock velocity was obtained as $v_s \propto \rho^{-0.45 \pm 0.02}$ and agreed well with a simple scaling obtained from the Hugoniot relation. X-ray shadowgraphy has shown a shock formation in porous targets and analysis suggests that there are two parts to compression waves: a shock front and a following pileup zone of multiple shock waves. Temporal histories of the pressure, the temperature, and the compression were estimated from the measured shock velocities and the opacities. It was found that the pressure peak due to the shock front was retarded to that by the pileup zone. The pileup zone had a higher compression and followed a thermodynamic condition closer to an adiabat than the shock front.

I. INTRODUCTION

A laser-driven shock wave propagates into a solid material ahead of the ablation front which is driven via thermal conduction from the absorbed laser energy. When the absorbed intensity changes in time, the ablation pressure changes accordingly. The time-dependent pressure generates successive shock waves during the laser irradiation, resulting in the creation of two parts of the shock compressed region: (i) a pileup zone in the rear portion of the shock wave where the incoming compression waves from the ablation surface pile up, and (ii) a steep shock front portion which is the front part of the shock wave propagating into the solid material ahead of the pileup zone.[1]

There have been many experimental studies of laser-driven shock waves, which were carried out using a visible-shadowgraph method with transparent targets[2] and shock breakthrough measurements with thin foil targets.[3,4] Most of them were based on measurements of only the shock front and it has been impossible to measure the pileup zone. Even with the thin foil techniques, it is difficult to investigate the pileup zone without a rarefraction effect since after the shock breakthrough the rarefaction wave overtakes the pileup zone from the rear side of the target and the temperature and the density must be changed.[5] There are few experimental studies of transient shock waves including the pileup zone. Such a detailed shock study would give assessments of the preheat in the shell as well as the shell dynamics depending on the time of shock breakthrough in inertial confinement fusion (ICF) targets. In a low density target a shock wave may become an important energy carrier since the fraction F_s of the absorbed energy used to sustain the shock wave depends on the target-mass density ρ_0 as $F_s \propto \rho_0^{-1/2}$.[6] In low density porous targets proposed especially for an ablator and/or a follow shell in ICF,[7] it is crucial for a high gain implosion to reveal details of the shock waves.

In this paper we present an extensive study of the laser-driven shock wave in deuterated polystyrene (CD) porous targets by using x-ray streak shadowgraphy. In a porous material, laser-driven shock waves were observed for the first time. Measurements and analysis indicated that the shock wave could be treated with the averaged density of foam and suggested that two parts of the compressed region be backlit by x-ray shadowgraphy. We attribute these to a shock front and a following pileup zone. The pileup zone has a compression higher than the shock front and follows a thermodynamic condition closer to an adiabat than the shock front. We also observed the time lag of the appearance of peak pressure between the shock front and the pileup zone. In Sec. II, the experiment is described. In Sec. III we show the experimental results including the dependence of the shock velocity and time-resolved profiles of the compression wave. In Sec. IV, we estimate the time-dependent shock parameters such as the pressure, the temperature, and the compression from the observed shock velocities and the opacities. The energy transport is also discussed. Finally, in Sec. V, we summarize the results and conclude our study.

II. EXPERIMENTAL CONDITION

The experiments were carried out with use of the GEKKO XII 12 beam laser system at the Institute of Laser Engineering, Osaka University.[8] The second harmonic (527 nm) of Nd-doped glass laser light was used with a temporally Gaussian pulse of 900 psec full width at half-maximum (FWHM). The temporal profile of the incident second harmonic light was monitored with an optical streak camera.

In Fig. 1(a) we show the experimental arrangement to measure directly a shock trajectory in a solid target with x-ray streak shadowgraphy. One beam of the GEKKO XII was focused on a surface of a CD ($[C_8D_8]_n$) foam slab target ($1.2 \times 1.2 \times 2.0$ mm) at normal incidence in order to drive a shock wave. The incident laser intensity was 3.3×10^{14} W/cm^2 at a spot diameter of 500 μm. Three other

 0899-8221/91/030735-10$02.00

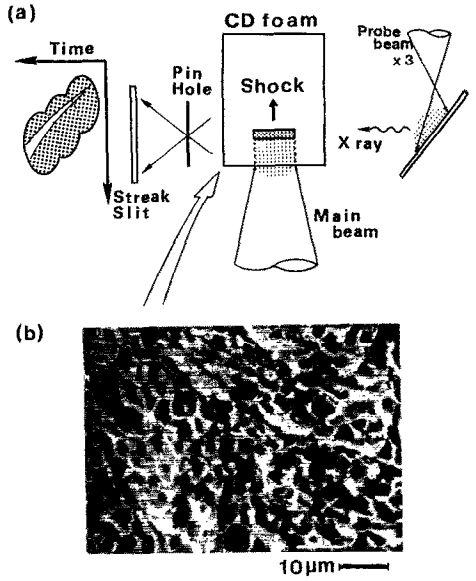

FIG. 1. Experimental configuration for measuring shock trajectories in a CD porous target. (a) The main beam was focused on CD porous targets with averaged-mass densities of 0.1 and 0.2 g/cm^3 at a laser intensity of 3.3×10^{14} W/cm^2. Only one backlighting beam is shown in the figure, while three beams were used at slightly different timings and positions. Probe x rays were imaged onto the entrance slit of an x-ray streak camera such that the shock propagation was along the slit direction. (b) A typical SEM picture of a used CD porous target. Each cell size is several microns.

beams were focused on a palladium (Pd) plate at an intensity of 10^{15} W/cm^2 to produce x-ray sources for the backlighting. Each beam was temporally delayed (-0.5, 0, and $+1$ nsec delay) compared with the main beam and was focused at a slightly different position to diagnose the moving shock trajectory in the foam target.

X rays from the Pd plasmas illuminated a foam target in the direction perpendicular to the main beam axis. The transmitted probing x rays were imaged onto the entrance slit of an x-ray streak camera through a 10 μm pinhole such that the shock propagation was along the slit direction. The temporal resolution of this system was calculated to be 80 psec. A gold photocathode was used for the x-ray streak camera with a 20 μm Be filter. Taking account of the effective quantum efficiency of the streak photocathode and Pd x-ray spectrum, the main photon energy of the detected x ray was about 3.1 ± 0.3 keV, which was emitted mostly from L-shell ions of Pd plasmas. The x-ray spectrum from the Pd plasma was monitored with a time-integrated crystal spectrograph. We took the snapshots without irradiating the Pd plate and did not observe emission from the overdense region. The streak sensitivity with the filter is matched to pass the L-shell line emission from a Pd plasma. High-Z material like Pd has a much higher emissivity than that of low-Z material such as plastic (CD foam). Besides, the temperature in the overdense region is too low ($\sim$50 eV) to emit the 3 keV photons.

Figure 1(b) shows a picture of a typical CD foam target with a scanning electron microscope (SEM). In the experiments 0.1 g/cm^3 and 0.2 g/cm^3 mass-density targets were used. The targets were fabricated by a freeze-dry method.[9] The average-mass density was estimated from the initial concentration of the CD polystyrene in a solvent taking account of a volume shrinkage rate of 10% during the freeze-dry process. In this way the accuracy of the mass density should be within about 20%.

Considering the temporal behavior of the shock wave induced by the ablation, it is important to know the time history of the absorbed laser intensity that should be coupled to the ablation pressure. The laser absorption was inferred from the difference between the incident and the scattered light energy. Time histories of back- and sidescattered light collected by the focusing lenses were measured with an optical streak camera in different irradiations but with the same experimental conditions. The energies of the back- and sidescattered light were monitored with five biplanar photo diodes at the same time, which showed the angular distribution of scattered light of $\cos^{4.1\pm1.6}$. The total nonabsorbed energy by integrating the scattered light energy over the solid angle gives a target absorption of $70\%\pm10\%$ for both cases of the target mass density (90.1 and 0.2 g/cm^3).

In order to compare the experimental results, we used the one-dimensional Lagrangian hydrodynamic code HISHO which used the LTE model and an EOS (equation of state) with an averaged atom model.[10] The EOS model does not include the effects of porosity which may relate to shock formation in porous material. The code includes multigroup electron and radiation transport and other conventional physics. The electron thermal energy was transported using a flux-limited diffusion flux and a free-streaming flux. The initial density of a porous target was treated as a homogeneous mass density.

III. EXPERIMENTAL RESULTS

Figure 2 shows a typical streak shadowgraph of the target with a mass density of 0.1 g/cm^3. The bright white region indicates the probing x rays transmitted through the target,

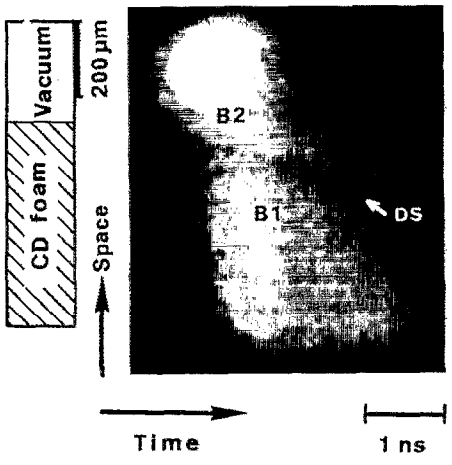

FIG. 2. Streak photograph (shadowgram) showing the shock wave propagation in a CD porous target with a mass density of 0.1 g/cm^3. The dark scar (DS) in the line corresponds to high density regions due to the shock wave. B1 and B2 are the bright regions at the front and the rear of the DS region, respectively.

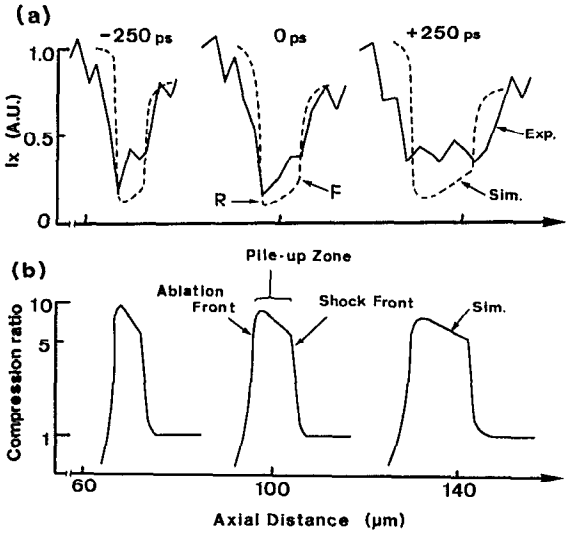

FIG. 3. Time resolved spatial profiles of a laser-induced shock wave. (a) Cross cuts of the relative x-ray intensity at the DS region in Fig. 2 along the spatial axis at three different times [− 250 (laser peak); 0, + 250 psec]. F and R are the front point rising sharply and the rear bottom point of the profiles, respectively. The solid line is from the experiment, while the dashed line is from the simulation. (b) Spatial distributions of the density compression ratio at − 250, 0, and + 250 psec from the simulation.

whereas the oblique dark scar indicates the region where backlighting x rays have been absorbed in the high density region created by a shock and a compression wave via laser ablation. The dark-scar (DS) region propagates into the target and the width broadens with time, indicating that a well-defined planar shock wave is created by laser ablation in the porous target. The bright (B-1) region in front of the DS region is the unperturbed area. Assuming negligibly small preheat, about 80% of the probe x ray (3 keV) should be transmitted through the B-1 region over a distance comparable to the laser spot diameter. The rear bright (B-2) region is the ablated region via electron thermal conduction where the electron temperature is above 100 eV and the x-ray transmittance should be about 100% in the laser spot area.

Figure 3(a) shows the scanned intensity along the spatial axis of the streaked data (Fig. 2) at three different times [− 250 (laser peak), 0, + 250 psec]. When the relative x-ray intensities are evaluated, the degradation of the original intensities due to the finite pinhole size (10 μm in diameter) is considered. By a simple image transformation scheme, the contrast of the image is corrected and has typically become 1.5 times higher than observed. From the 1-D simulation results spatial distributions of the relative x-ray intensity and the density compression ratio in the shock compressed region are also shown as the dashed line in Fig. 3(a) and the solid line in Fig. 3(b), respectively. In calculating the relative x-ray intensity, it was assumed that the lateral distance of the compression region in the target is equal to the laser spot diameter (500 μm). More details of the simulation condition are presented in Sec. IV.

The simulated profiles of the compressed region indicate that the shock wave induced by the ablation pressure arrives at the rear side of the compression wave, resulting in two regions: (1) a multiple shock or pileup zone at the rear side, and (2) a shock front propagating into the material ahead of the pileup zone. In the x-ray intensity profiles [dashed lines in Fig. 3(a)] from the calculation, the front portion rising sharply (F) and the rear bottom point (R) correspond to the shock front and the density maximum in the pileup zone in Fig. 3(b), respectively, in each time step. The opacity near the R point (ablation region) changes abruptly where the density drops and the temperature increases rapidly.

Comparing the experimental intensity profiles with the calculation, the experimental ones are quite close to the calculation except for some detailed structures. The profile from the experiment broadens with time as do the ones from the calculation. The x-ray intensity profile, characteristic of a pileup zone between the F and R points shown in Fig. 3(b), appeared in all experiments but the high frequency structures in the region were not reproducible. A laser-induced strong shock wave is generated in the overdense region (electron density $n_e \sim 10^{23}$ cm^{-3}) by the ablation pressure. The ablation pressure is applied at the ablation front ($n_e \sim 3\times10^{22}$–4×10^{23} cm^{-3}) by thermal electrons via heat conduction from the critical point ($n_e = 4\times10^{21}$ cm^{-3}). Laser energy is deposited at the critical point. Scattered light comes from the critical point or the underdense region. Hence the shock wave created in the overdense region must not directly correlate with the scattered light. Any temporal oscillations in scattered light are usually due to nonlinear couplings of laser (electron magnetic) and plasma (electron static) waves. Thus the detailed structures in the x-ray profile may not indicate correlation with the laser pulse modulation. These structures must come from the cathode of the streak camera and/or backlight source modulation. The intensity decrease of the R point at + 250 psec may be due to the rarefaction wave generated at the ablation front after the laser peak. Simulation results also indicate the presence of a rarefaction, which causes the transmitted x-ray intensity at + 250 psec to be higher than the one at the laser peak as shown in Fig. 3(a). The change of the transmitted x rays in the experiment is larger than that from the one-dimensional (1-D) simulation. Such a discrepancy may come from the lateral rarefaction effect at the ablation front. Taking into account the errors in the absolute intensities, it is quite possible that the F and R points in the experiment [solid lines in Fig. 3(a)] correspond to the shock front and the rear part of the pileup zone, respectively. The intensity profile due to the finite resolution in the imaging system may affect the intensities to be reduced as mentioned earlier. A three-dimensional (3-D) expansion of a shock wave may also be responsible for the intensity discrepancy with time lapse. The 3-D expansion of a shock wave by a lateral rarefaction affects the one-dimensional shock wave and changes the x-ray transmission through the shock perturbed region. Assuming that the edge rarefaction enters at an angle of approximately 45°,[11] the transmitted x-ray intensity with the rarefaction increases at most twice at the axial distance of 150 μm compared with the purely one-dimensional case. The corresponding changes in the shock parameters are evaluated in the following discussion (Sec. IV D). Another possible effect of the 3-D expan-

sion is that the edge rarefaction may interfere with a shock wave and may reduce the shock front speed in the observed region. However, the edge rarefaction should not affect the shock front up to the axial distance of 200 μm, considering the 45° edge rarefaction.

Henderson *et al.*[12] have also presented results indicating an increase of the shock thickness due to the porous effect. According to this reference the DS region in Fig. 2 could correspond to the shock thickness or broadening into a compression wave.[12] We also measured the shock front property by observing the time-resolved rear emission of a laser-irradiated thin foam target, the thin foil technique, which is well known and established.[3,4] The rear side emission was measured with a visible streak camera coupled with a Schwarzschild microscope. The system spectral response was from 380 to 480 nm and the intensity response was calibrated. Figure 4 shows the temporally resolved rear side emissions with (a) a polystyrene foam target (70 μm) and (b) an Al solid target (20 μm). The temporal fast rise peak of the foam target corresponds to the shock front because the temporal profile (foam) in Fig. 4(b) is similar to that (Al) in Fig. 4(a) where the fast rise peak has been confirmed as the shock front.[3,4] The rear side emission ensures that the shock front is really created in the foam target.

Figure 5 shows the positions of the F and R points versus time for targets with densities of 0.1 and 0.2 g/cm^3. Two data sets for each density target were taken at the same experimental condition. The two data sets were almost identical. At an early time of the laser pulse the F and R points are accelerated but after about the laser peak the F point becomes a steady state for both target densities. At an early time of the laser pulse, the ablation pressure increases with the laser intensity and time, resulting in the acceleration of the shock wave.

The distance between the R and F points is expanded as they propagate deeper into the target (this expansion is also

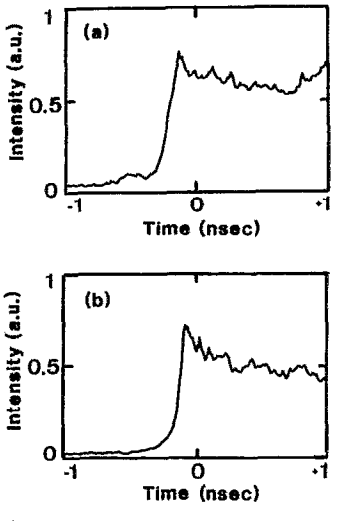

FIG. 4. Temporal histories of the rear side emission with (a) a polystyrene foam target (70 μm) and (b) an Al target (20 μm). The spectral range of the emission was from 380 to 480 nm. Time zero corresponding to the laser peak of the incident pulse was determined with an optical time fiducial.

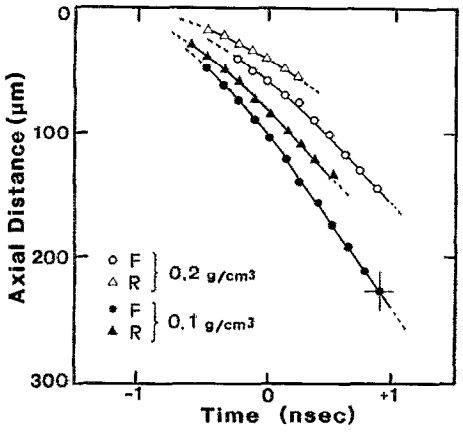

FIG. 5. Shock wave positions (F and R points) versus time for two different mass-density targets of 0.1 and 0.2 g/cm^3. Open circles and triangles are the R and F points for 0.2 g/cm^3 density targets. Closed circles and triangles are the R and F points for 0.1 g/cm^3 density targets.

seen in Figs. 2 and 3). The velocity of the F point is higher than the R point. When the ablation pressure increases (case A), the virtual piston (say, the ablation front) creates a pileup zone with multiple shock waves and the density should be highest in the front of the piston. The shock front runs ahead of the pileup zone, its speed being typically higher than the piston. After the maximum of the ablation pressure, i.e., after the laser peak (case B), the shock front velocity becomes steady until the rarefaction wave catches up. At this time the rear of the pileup zone begins decelerating because of the rarefaction. In either case of A or B, the velocity of the rear part of the pileup zone is generally lower than the shock front.[13] Consequently, the difference of the velocities between the shock front and the pileup zone causes the broadening of the compression wave. These propagation characteristics (Fig. 5) and the intensity profiles (Fig. 3) suggest that the R and F points correspond to the rear part of the pileup zone and the shock front, respectively.

At steady state, the shock front velocities of 0.1 g/cm^3 and 0.2 g/cm^3 targets are 1.5×10^7 and 1.1×10^7 cm/sec, respectively. Here the absorbed laser intensities for the different mass-density targets were the same within $\pm 8\%$. These experimental results indicate that the dependence of the shock front velocity (v_f) on the target mass density (ρ_0) is $v_f \propto \rho_0^{-0.45\pm0.02}$. Theoretical scaling of the shock front velocity at a steady state is simply from the equation of mass and momentum conservation across the shock front:

$$v_f = [\rho_f/(\rho_f-\rho_0)]^{1/2}\cdot P^{1/2}\cdot\rho_0^{-1/2}, \quad (1)$$

where P, ρ_0, and ρ_f are the pressure, the initial density, and the compressed density by the shock wave, respectively. The scaling from the 1-D simulation was the same as the theoretical one. The shock front speed in a normal density Al target ($\rho = 2.69$ g/cm^3) was also measured by the thin foil technique as mentioned above to be $3.5\pm0.5\times10^6$ cm/sec. Even with some laser absorption difference between the Al and polystyrene targets, the target density scaling of shock speed with the foam target is consistent with the result of the Al target. These experimental results and simulation indi-

cate that a shock wave is really created in the porous target and can be treated as a fluid based on the average density in our experiment.

IV. DISCUSSION

A. Data analysis

With the above x-ray shadowgram, we can obtain the opacity and the velocity of the shock front and the pileup zone. In general, the opacity (τ) is a function of temperature (T_e) and the density (ρ) as $\tau = f(T_e,\rho)$. Inferring the temperature, we can estimate the density with some function of the opacity and the pressure (P) by applying an equation of state (EOS) such as a relation of $P = g(T_e,\rho)$.

A pure shock wave satisfies the Hugoniot relation in a steady state. With the acceleration of a shock front, the front may not completely satisfy the Hugoniot relation. However, considering an infinitesimal time interval, abrupt changes of the shock front parameters are small during the short interval. Then we can treat a shock front with an acceleration in a quasisteady state. Between the regions ahead of and behind the shock front, the pressure jump is large enough ($P_f/P_0 \gg 1$) and the entropy changes suddenly. Furthermore, the shock front here is always facing and propagating into the unperturbed region of solid material unless there is any anomalous energy transport before the shock. Then thermodynamic trajectory in the P-ρ plane of the front part is generally quite close to the Hugoniot condition. Thus we may apply the Hugoniot relation $P = h(v_f,\rho_f)$ of Eq. (1) for a quasisteady state to the shock front (quasisteady model). The five parameters (v_f, T_f, P_f, ρ_f, and τ_f) in the shock front portion are related by the above three functions (f, g, and h). From the experiment we can obtain two parameters (v_f, and τ_f). Using the above functions, we can estimate the other three parameters (T_f, P_f, and ρ_f) as shown in Appendix A.

The rear portion, namely the pileup zone, of the compression wave behaves quite differently compared with the shock front. The pressure and the density in the pileup zone change successively in space and the entropy change is smaller than that of the shock front. The thermodynamic trajectory in a P-ρ plane of the pileup zone should be somewhere between the Hugoniot and adiabatic conditions and can be described as[1]

$$P(t) = P_0(\rho(t)/\rho_0)^{\alpha} \tag{2}$$

For an adiabatic condition, α is equal to the adiabatic constant γ which is $\frac{5}{3}$ for an ideal gas, and Eq. (2) is the Poisson adiabatic equation.[13] In the pileup zone, α becomes larger than γ. It is shown in Appendix B that when the compression motion has a constant acceleration, one obtains the temporally changing pressure of the pile up zone as a function of the density and the velocity:

$$P(t) = [P(0)/\rho(0)]v_0^{-2}(v_0 + at)^2\rho(t)$$
$$= (1/\alpha)v(t)^2\rho(t), \tag{3}$$

where $P(0)$, $\rho(0)$, and v_0 are the pressure, the compressed density, and the velocity at a given time $t = 0$. This feature is satisfied not only in the pileup zone but also in the shock front portion of an acceleration phase.

If we take $v(t)$ in Eq. (3) as the shock wave velocity, Eq. (3) is satisfied only for an acceleration phase and not for a deceleration phase or a rarefaction wave. However, as shown in Fig. 3, the R point in the pileup zone is quite close to the ablation surface which works as a piston producing a shock wave. Then it is reasonable to assume that the velocity of the R point is almost equal to the piston velocity. In this assumption Eq. (3) is also extended extensively to a deceleration phase as shown in Appendix B. Therefore, even if the portion follows with a variable acceleration or deceleration, we are able to use Eq. (3) for quasiconstant acceleration or deceleration within an infinitesimal time interval (quasiconstant acceleration model). Using Eq. (3) and an EOS we can estimate the pressure, the temperature, and the compression of the R point from the obtained velocity and the opacity data as shown in Appendix A for a quasiacceleration model.

B. Shock front property

Figure 6(a) shows the temporal behaviors of the shock front velocity and the compression ratio of the shock front density ρ_s to the initial density ρ_0 for a 0.1 g/cm^3 density target. The time histories of the temperature and the pressure at the shock front are shown in Fig. 6(b). These parameters are evaluated with the quasisteady model.

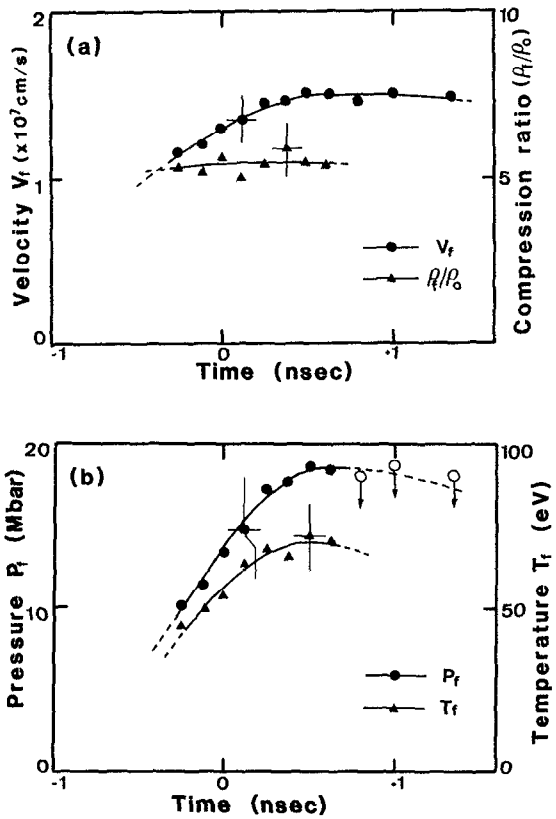

FIG. 6. Shock front property evaluated with streak data and the quasisteady model. (a) Temporal behaviors of F-point (shock front) velocity (v_f) and compression ratio (ρ_f/ρ_0) to the initial density for a 0.1 g/cm^3 density target. Closed circles and triangles are v_f and ρ_f/ρ_0. (b) Time histories of the temperature (T_f) and the pressure (P_f) of the F point. Closed circles and triangles are P_f and T_f. Open circles are implied for the compression ratio of 5.5 and indicate the maximum limit.

Two phases are clearly seen in Fig. 6(a) or in the time history of the shock front velocity: (i) a phase of acceleration, and (ii) a phase of constant velocity. The shock front travels with a near constant acceleration of 5×10^{15} cm/sec^2 until about 500 psec after the laser peak and a final velocity of 1.5×10^7 cm/sec is attained. A detailed acceleration property in the early time of the laser pulse has not been observed experimentally but the acceleration should vary during the rise of the laser pulse according to the simulation. If the shock front would behave as a single shock wave satisfying the Hugoniot relation, there would be no acceleration of the shock front. Thus we have to deduce the shock parameters of an acceleration phase from the quasiconstant acceleration model. However, the pressure deduced from the quasiconstant acceleration model [Eq. (3)] is similar to that from the quasisteady model [Eq. (1)] within 10%. Then the exponent α in Eq. (2), which indicates the thermodynamic property in the P-ρ plane, was more than 7. Here α can be estimated by Eq. (B9). The time history of the compression ratio indicates that the compression ratio is almost constant at about 5.5 in the acceleration. Even during an acceleration phase, the thermodynamic condition in the shock front is close to the Hugoniot curve in the thermodynamic trajectories and is near the limit of the strong shock condition ($P_s/P_0\gg1$). Thus the results of the pressures from both models and the time history of the compression ratio indicate that it is reasonable to apply the quasisteady model in the shock front portion to this experimental condition.

The temperature and pressure at the shock front increase during the shock acceleration as shown in Fig. 6(b). The maximum pressure and temperature become 19 Mbar and 72 eV, respectively, at 500 psec after laser peak. In general, the ablation pressure also increases with laser intensity but reaches its maximum at the laser peak. Such a time delay of the peak pressure at the shock front is due to the finite traverse time from the ablation front to the shock front. More detail of this delay will be presented in the following discussion (Sec. IV D).

To show the applicability of the EOS model in our data processing, we estimate the temperature here using an EOS for ideal plasmas. In the observed temperatures and densities, the plasma at the shock front should be nondegenerate since the Fermi temperature is estimated to be about 10 eV, which is smaller than the estimated electron temperature (50–70 eV) at the shock front.[14] The ion coupling parameter Γ, which is the ratio of the screening energy to the thermal energy,[15] is estimated to be $\Gamma\leqslant1$ for the temperature $T_e\geqslant50$ eV. These results may imply that the plasma at the shock front is close to the ideal plasma condition.[14] For the ideal plasma approximation, the pressure is given by an EOS in a partially ionized gas as

$$P=P_e+P_i+P_r\simeq n_ikT_i+n_ekT_e \simeq\rho_s[(z+1)/Am_p]kT, \quad (4)$$

where P_e, P_i, and P_r are the electron, ion, and radiation pressures, respectively. The radiation pressure is dropped here because the value is negligibly small (only 0.006% of the total plasma energy is estimated to be used for the radiation). Combining Eqs. (1) and (4), the temperature is given by the shock velocity as

$$kT=\left(\frac{Am_p}{(z+1)}\right)\frac{1-1/K}{K}v_s^2, \quad (5)$$

where $K=\rho_f/\rho_0$ (compression ratio). For $K=4$ ($\gamma=\frac{5}{3}$), the velocity of 1.5×10^7 cm/sec leads us to estimate the temperature to be 77 eV at the average charge state of $Z=3$. If K is larger [for example, 5.8, which corresponds to the maximum points of the compression ratio in Fig. 6(a)], the temperature becomes lower (59 eV) than the above value. This level of the temperature (59–77 eV) is estimated with the assumption of the ideal plasma condition. The temperature above is quite consistent with the peak temperature (72 eV) in Fig. 6(b) where information about the opacity is included. Thus it is proved that with our experimental conditions the shock front is close to an ideal plasma condition.

C. Pileup zone property

Figure 7 shows the temporal behaviors of the velocity, compression ratio, pressure, and temperature estimated from the quasiconstant acceleration model at the R point for a 0.1 g/cm^3 density target. It is found that there are two

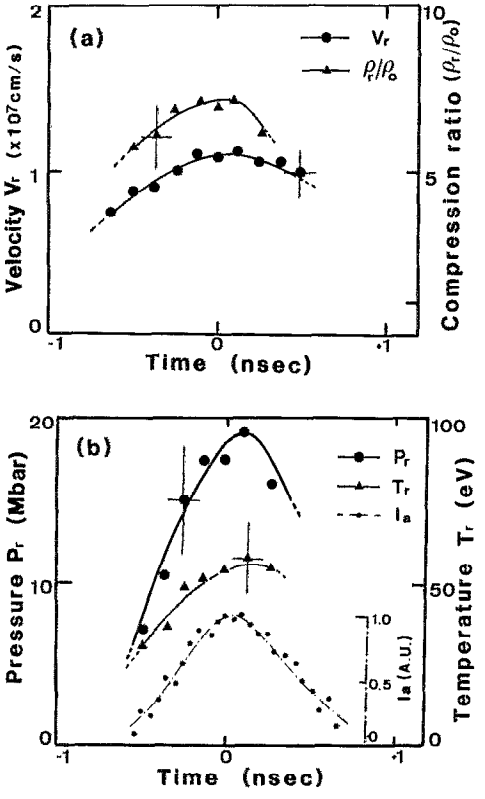

FIG. 7. Pileup zone property estimated from the streak data and the quasiconstant acceleration model. (a) Temporal behaviors of R-point (pileup zone) velocity (v_r) and compression ratio (ρ_r/ρ_0) to the initial density for 0.1 g/cm^3 density targets. Closed circles and triangles are v_r and ρ_r/ρ_0. (b) Time histories of the temperature (T_r) and the pressure (P_r) of the R point. Closed circles and triangles are P_r and T_r. Small closed circles are the relative absorbed laser intensity (I_a). The profile of the dot-dashed line in the first half is approximated as 750 psec near Gaussian. The pressure profile of the solid line is given by Eq. (7) for $\beta=0.55$ or $P_r(t)\propto I_a^{0.55}$.

different phases in the time history of the velocity before and after the laser peak: (i) a phase of acceleration, and (ii) a phase of deceleration.

During the phase of acceleration, the compression [Fig. 7(a)], the temperature [Fig. 7(b)], and the pressure [Fig. 7(b)] increase with time. Though the compression at the shock front portion is almost constant at 5.5 in the acceleration phase as in Fig. 6(a), the compression ratio at the R point changes from 5.7 to 7 and is larger than the value in the shock front region. At the R point, multiple shock waves are created where the incoming shock waves from the ablation surface pile up. This part has a higher compression than the shock front portion. The exponent α (the thermodynamic property) in Eq. (2) is from 2.5 to 4; its magnitude is smaller than that of the shock front portion ($\geqslant 7$) and larger than the adiabatic constant γ ($\frac{5}{3}$ for ideal gas). The compression at the pileup zone is closer to an adiabatic condition than that in the shock front region and satisfies the approximate Hugoniot condition. The maximum temperature (57 eV) at the R point is lower than that (72 eV) of the shock front in spite of the fact that both regions have the same magnitude of maximum pressure. This is also consistent with the adiabatic condition. In the pileup zone, the successively increasing ablation generates weak shock waves and multiple shock waves pile up. Then the pressure at the pileup zone gradually changes in an infinitesimal spatial interval and the R point is compressed with a small change of the entropy.

During the deceleration phase, the density, temperature, and pressure decrease. When the absorbed laser intensity decreases, the pressure at the ablation surface drops. Then the rarefaction wave propagates into the target, eventually overtaking and attenuating the shock wave in the pileup zone.

The pressure behavior at the R point in the pileup zone is temporally different from that of the shock front. The temporal profile of the R-point pressure should be close to that of the ablation pressure since the R point is spatially close to the ablation front until 250 psec after the laser peak, as shown in Fig. 3. The ablation pressure generally depends on the absorbed laser intensity and is simply described as the scaling of $P_a \propto I_a^{\beta}$, where β is a constant and depends on the ablation model.[4,6,16,17] The absorbed laser intensity profile obtained from the experiment is also shown in Fig. 7(b) as a dot-dashed line. The first half of the absorbed laser intensity can be approximated with a Gaussian 750 psec FWHM as

$$I(t) = I_0 \exp[-4 \ln 2(t(\text{psec})/750)^2] . \quad (6)$$

Thus the pressure at the pileup zone will be given by

$$P(t) = P_{\max} \exp[-4 \ln 2\beta(t(\text{psec})/750)^2] . \quad (7)$$

The data points are fitted with Eq. (7), using $\beta = 0.55$ as shown in Fig. 7(b) using a solid line connecting the closed circles. The intensity dependence of the pressure is obtained as $P \propto I_a^{0.55}$ from the figure. This scaling is in good agreement with the ablation pressure scaling reported in the previous experimental results with plane targets.[17] Thus we conclude that the pressure characteristics at the R point reflect those of the ablation front.

D. Energy transport

From the above data analysis of the shock front and the pileup zone, 19 Mbar of ablation pressure is attained. However, 1-D simulation gives a peak pressure of 29 Mbar for the experimental condition here with the flux limiter $f = 0.6$, where the predicted absorption in the simulation is in agreement with the measured one within the experimental errors. Even with a very limited flux of $f = 0.03$, the predicted ablation pressure drops only to 26 Mbar, still much larger than the measured one. The ambiguity of the observed x-ray intensity, which stems from the degradation due to the finite spatial resolution and/or the 3-D effect of the edge rarefaction, may underestimate the density and the pressure. Suppose that the observed x-ray intensity through the shock perturbed region is two times lower than the original transmitted intensity, and the observed pressure rises to 25 Mbar. However, this forced factor of two reduction of the x-ray intensity exceeds the experimental error. The reported scalings of the ablation pressure including lateral energy loss with planar targets or with small spot diameter experiments give a range of pressures from 12.4 to 18.5 Mbar with our experimental condition.[17] The lateral heat loss is likely to be one of the important factors for explaining the discrepancy of the peak pressure between the experiment and the 1-D simulation, though we have not checked this using 2-D simulations. If the code is run at 74% of the absorbed energy (in other words the other 26% is thrown away for the lateral energy loss), the shock trajectory from the simulation achieves good agreement with the experiment. At this simulation condition, the peak pressure and compression ratio at the R point are 20–21 Mbar and 8.3–8.8, respectively, when the temperature is 55–60 eV. The simulated temperature is close to the experimental one (57 eV) while the compression from the experiment (7) is lower than the simulation. The porosity effect may also be one of possible mechanisms for explaining the discrepancy between the experiment with the porous targets and the simulation with average density material. It has not been confirmed whether the porosity is responsible for the above discrepancy from the experimental observation.

From Figs. 6(b) and 7(b) the pressure profile of the F point is delayed compared with that of the R point and the time lag increases with time. The pressure at the F point maximizes at 500 psec after the laser peak but the peak pressure at the R point appears only at 100 psec after the laser peak. Such a time lag of the peak pressure indicates the finite traverse time for the shock propagation through the compression region. The temporal change of the time lag is due to the increase of the distance between the R and the F points with time as shown in Figs. 3 and 5. In a moving frame of the shock compressed region between the F and R points, each one of the multiple shock waves travels successively and adiabatically from the R to F points. Then the pressure information created at the ablation surface is transported to the shock front region with an order of the sound speed since in the limit of a weak shock the entropy approaches zero $(P_1 - P_0)/P_0 \to 0$ and the wave speed is equal to the sound speed in the moving frame (between the R and F point).[13] For this time lag (400 psec) and the traverse distance (25

μm) between the F and R points, the corresponding speed is estimated to be 6×10^6 cm/sec. This value is equivalent to the sound speed of a plasma temperature of 65 eV with an average charge state $Z=3$. This averaged temperature between the F and R points from $+100$ psec to $+500$ psec is in good agreement with the estimation of the temperatures as shown in Figs. 6(b) and 7(b). This agreement indicates that in the compressed region (pileup zone) from the R to F points the entropy change is small and the thermodynamic condition is closer to the adiabat than the Hugoniot condition.

Finally we consider the fraction F_s of the absorbed energy used to sustain the shock wave. The energy flux I' resulting from the work done by the shock pressure P is $I'=Pu$, where u is the fluid velocity behind the shock front deduced from the conservation of mass and momentum across the shock front as $u=(1-1/K)v_s$. Then F_s is identified with I' relative to the absorbed laser intensity I_a as

$$F_s=\frac{I'}{I_a}=\left(1-\frac{1}{K}\right)\frac{Pv_s}{I_a}. \tag{8}$$

For our measured conditions ($P=18$ Mbar, $v_s=1.5\times10^7$ cm/sec, $K=5.5$, and $I_a=2.1\times10^{14}$ W/cm^2), we obtain $F_s=10\%$. Other energy fluxes of the absorbed flux will be used for the creation of axial thermal conduction, outward kinetic energy, and lateral heat loss.

V. SUMMARY AND CONCLUSIONS

Laser-induced shock wave propagation in CD porous targets was observed with x-ray streak shadowgraphy. Target average-mass densities of 0.1 g/cm^3 and 0.2 g/cm^3 were used. The final shock wave velocities were 1.5×10^7 cm/sec and 1.1×10^7 cm/sec, respectively. The density scaling of the velocity was $v_s\propto\rho^{-0.45\pm0.02}$, whose scaling was consistent with a shock speed measured in normal density Al targets and was also in good agreement with a simple scaling from the Hugoniot relation. Such a result indicates that a shock wave is created in the CD porous target with our experimental condition. The x-ray shadowgraphy shows clearly a shock formation in the porous targets, which is composed of two parts: a shock front and a following pileup zone of multiple shock waves. Using a quasisteady model for the shock front and a quasiconstant acceleration model for the pileup zone, temporal histories of the temperature, the pressure, and the compression ratio at two different points are estimated from the measured shock velocities and the opacities. Maximum temperature and pressure at the shock front for the 0.1 g/cm^3 targets are estimated to be 70 eV and 19 Mbar, respectively. The same maximum pressure is attained in the pileup zone but the compression ratio (ρ/ρ_0) and the temperature (T_e) in the pileup zone ($\rho/\rho_0=5.7$–7 and $T_e=57$ eV) are higher and lower than those of the shock front ($\rho/\rho_0=5.5$ and $T_e=72$ eV). The temporal profile of the pressure at the shock front also differs from that of the pileup zone. The pressure at the pileup zone reaches its maximum at about the peak of the absorbed laser intensity. The temporal profile indicates the absorbed laser intensity scaling as $P\sim I_a^{0.55}$, the same as the reported ablation pressure scaling. However, the pressure at the shock front is delayed and reaches its maximum at 400 psec after the peak of the pileup zone pressure. This time delay is due to the finite traverse time of the shock from the ablation to the shock front. The time lag of the peak pressure between the shock front and the pileup zone gives temperature in the shock compressed region. Assuming a small entropy change in the compressed region (pileup zone), the temperature (65 eV) deduced from this time lag is consistent with the result (57–72 eV) from the shock velocity and the opacity. Comparing the shock parameters and the temporal profiles of the pressure between the shock front and the pileup zone, it is concluded that the pileup zone followed a thermodynamic condition closer to the adiabat than the shock front.

ACKNOWLEDGMENTS

We are indebted to Dr. C. Yamanaka, Dr. Y. Kato, Dr. M. Nakatsuka, Dr. T. Jitsuno, Mr. M. Takagi, and Dr. T. Kanabe. This study would not have been possible without the technical support from the members of the GEKKO laser operation and devices, the plasma diagnostics and measurement, and the target fabrication groups. Their contributions are gratefully acknowledged.

APPENDIX A: EOS FOR DATA ANALYSIS

Figure 8 shows the calculated results of the EOS (lines) with the various temperatures obtained from the well-known averaged atom model (AAM)[18] for CD material with a 0.1 g/cm^3 mass density. The dotted line indicates a trajectory according to Eq. (1) for a shock velocity obtained with the experiment (in this case $v_f=1.5\times10^7$ cm/sec is used). The temperatures expressed on the dotted line are determined by the obtained opacity. The temperature on this dotted line frame increases with the compression ratio for a given opacity, since the opacity depends on the density and temperature. Assigning the cross point of the two curves

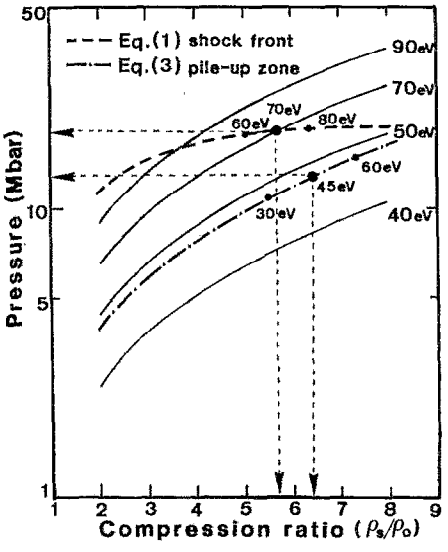

FIG. 8. Thermodynamic trajectories (lines) with various temperatures from AAM for CD material with 0.1 g/cm^3 mass density. Dotted and dot-dashed lines are given by Eqs. (1) and (3), respectively. The temperatures expressed on the bold dotted and dot-dashed lines are obtained from the experiment (opacity).

with the same value of temperatures as the real temperature, we have a unique solution for the pressure and the compression.

The dot-dashed line in Fig. 8 is given by Eq. (3) for a definite velocity and α. As shown in Fig. 8 the temperature can be determined uniquely within a 10% accuracy from the obtained opacity for the same reason as above.

APPENDIX B: THERMODYNAMIC TRAJECTORY OF THE PILEUP ZONE FOR A QUASICONSTANT ACCELERATION MODEL

When a compression wave's motion has a constant acceleration, the time evolution of the pressure and the density in the pileup zone has been solved as shown in Refs. 1 and 13. If the thermodynamic trajectory of the discontinuity is from one Hugoniot curve to another, the instantaneous shock velocity is found as

$$v_s^2(t) = V^2(t-\Delta t)\{[P(t) - P(t-\Delta)]/[V(t-\Delta t) - V(t)]\}, \tag{B1}$$

where v_s, V, and P are the shock velocity, volume, and pressure, respectively. For $\Delta t \to 0$, Eq. (B1) is modified to

$$v_s^2(t) = -V^2(t)[\dot{P}(t)/\dot{V}(t)] = \dot{P}(t)/\dot{\rho}(t). \tag{B2}$$

When compression wave motion has a constant acceleration (a), Eq. (B2) is described as

$$\frac{dP}{dt} = (at + v_0)^2 \frac{d\rho}{dt}. \tag{B3}$$

Substituting Eq. (2) into Eq. (B3), we obtain the time evolution of the pressure and density:

$$\rho(t) = \rho(0)(1 + at/v_0)^{2/(\alpha-1)}, \tag{B4}$$

$$P(t) = P(0)(1 + at/v_0)^{2\alpha/(\alpha-1)}. \tag{B5}$$

Equations (B4) and (B5) yield

$$P(t) = [P(0)/\rho(0)]v_0^{-2}(v_0 + at)^2\rho(t). \tag{B6}$$

Assuming a thermodynamic relation $P = p[\rho(t)]$, the time derivatives satisfy $\dot{P} = (\delta p/\delta\rho)\cdot\dot{\rho}$, and (B3) yields

$$\delta p/\delta\rho = (at + v_0)^2. \tag{B7}$$

Partially differentiating Eq. (2), Eq. (B7) is modified to

$$\alpha(P_0/\rho_0^\alpha)\rho(t)^{\alpha-1} = (at + v_0)^2. \tag{B8}$$

Using Eqs. (2) and (B8) for $t = 0$ we obtain the relation

$$[P(0)/\rho(0)]v_0^{-2} = 1/\alpha. \tag{B9}$$

The above treatment is not satisfied for a deceleration phase of the velocity. However, assuming that the velocity of the pileup zone v_s is equal to a piston velocity U_p which creates a shock wave or rarefaction wave, the above results can be extended to the deceleration condition. In the piston model the change of the piston velocity creates a discontinuity of the pressure and the density at the front of the piston as

$$U(t) - U(t-\Delta t) = j\{[P(t) - P(t-\Delta t)] \times [1/\rho(t-\Delta t) - 1/\rho(t)]\}^{1/2}, \tag{B10}$$

where $j = \pm 1$, i.e., positive or negative. When $j = +1$, (B10) indicates that the piston is accelerated and a compression wave is created. When $j = -1$, the piston is decelerated and a rarefaction wave is created. In any case, for $\Delta t \to 0$, Eq. (B10) is modified to

$$\left(\frac{dU}{dt}\right)^2 = \rho(t)^{-2}\frac{dP}{dt}\frac{d\rho}{dt}. \tag{B11}$$

Using Eq. (2) and (B11), we obtain

$$\frac{dU}{dt} = A\rho(t)^{(\alpha-3)/2}\frac{d\rho}{dt}. \tag{B12}$$

Equation (B12) gives similar results on the time evolution of the pressure and the density, when compared with Eq. (B4) and Eq. (B5), as

$$\rho(t) \propto U(t)^{2/(\alpha-1)}, \tag{B13}$$

$$P(t) \propto U(t)^{2\alpha/(\alpha-1)}. \tag{B14}$$

Then, even in the piston model we can obtain the same relation for the pressure, density, and velocity as in Eq. (B6).

[1] D. Saltzman, S. Eliezer, A. D. Krumbein, and L. Gitter, Phys. Rev. A **28**, 1738 (1983).

[2] C. G. M. van Kessel and R. Sigel, Phys. Rev. Lett. **33**, 1020 (1974); D. Billon, D. Cognard, J. Launspach, C. Patou, D. Redon, and D. Scirmann, Opt. Commun. **15**, 108 (1975); F. Amiranoff, R. Fedosejevs, R. F. Shmalz, R. Sigel, and Y. L. Teng, Phys. Rev. A **32**, 3535 (1985); A. Ng, P. Celliers, and D. Parfeniuk, Phys. Rev. Lett. **58**, 214 (1987).

[3] L. R. Veeser and J. C. Solem, Phys. Rev. Lett. **40**, 1391 (1978); R. J. Trainor, J. W. Shaner, J. M. Auerbach, and N. C. Holmes, Phys. Rev. Lett. **42**, 1154 (1979); E. A. McLean, S. H. Gold, J. A. Stamper, R. R. Whitlock, H. R. Griem, S. P. Obenschain, B. H. Ripin, S. E. Bodner, M. J. Herbst, S. J. Gitomer, and M. K. Matzen, Phys. Rev. Lett. **45**, 1246 (1980); F. Cottet, J. P. Romain, R. Fabbro, and B. Faral, Phys. Rev. Lett. **52**, 1884 (1984); A. Ng, D. Parfeniuk, L. DaSilva, and D. Pasini, Phys. Fluids **28**, 2915 (1985).

[4] A. Yamauchi, K. A. Tanaka, R. Kodama, M. Kado, T. Yamanaka, T. Mochizuki, S. Nakai, and C. Yamanaka, Appl. Phys. Lett. **52**, 786 (1988); K. A. Tanaka, A. Yamauchi, R. Kodama, T. Yabe, T. Mochizuki, T. Yamanaka, S. Nakai, and C. Yamanaka, J. Appl. Phys. **65**, 5068 (1989); R. Fabbro, B. Faral, J. Virmont, F. Cottet, P. Romain, and H. Pepin, Phys. Fluids **28**, 3414 (1985).

[5] L. DaSilva, A. Ng, and D. Parfeniuk, J. Appl. Phys. **58**, 3634 (1985).

[6] R. Fabbro, C. E. Max, and E. Fabre, Phys. Fluids **28**, 1463 (1985).

[7] R. Mason, Nucl. Fusion **15**, 9 (1975); R. A. Sacks and D. H. Darling, Nucl. Fusion **27**, 447 (1987); K. Okada, T. Mochizuki, S. Sakabe, H. Shiraga, T. Yabe, and C. Yamanaka, Appl. Phys. Lett. **43**, 231 (1983).

[8] C. Yamanaka, S. Nakai, T. Yamanaka, Y. Izawa, Y. Kato, K. Mima, K. Nishihara, Y. Mochizuki, M. Yamanaka, M. Nakatsuka, T. Sasaki, T. Yabe, K. Yoshida, H. Azechi, H. Nishimura, T. Norimatsu, S. Ido, N. Miyanaga, S. Sakabe, H. Takabe, J. Jitsuno, and M. Takagi, Nucl. Fusion **27**, 19 (1987).

[9] T. Norimatsu, H. Katayama, T. Mano, M. Takagi, R. Kodama, K. A. Tanaka, Y. Kato, T. Yamanaka, and S. Nakai, J. Vac. Sci. Technol. A **6**, 3144 (1988).

[10] M. Murakami and K. Nishihara, ILE Q. Prog. Rep. **6**, 34 (1983).

[11] R. M. More, in *Proceedings of the 5th Workshop on Laser Interactions and Related Plasma Phenomena* (Plenum, New York, 1981), Vol. 5, p. 253.

[12] L. F. Henderson, P. Colella, and G. Puckett, in *Proceedings of the 17th International Symposium on Shock Waves and Shock Tubes* (AIP, New York, 1989), p. CF.1.

[13] B. Ya. Ze'ldovich and Yu. P. Raizer, *Physics of Shock Waves and High Temperature Hydrodynamic Phenomena* (Academic, New York, 1966).

[14] R. M. More, in *Proceedings of the 29th Scottish University Summer School in Physics* (Camelot, Southampton, 1985), p. 157.

[15] S. Brush, H. Sahlin, and E. Teller, J. Chem. Phys. **45**, 2102 (1966); J. P. Harsen, Phys. Rev. A **8**, 3096 (1973); M. Baus and J. P. Harsen, Phys.

Rep. **59**, 1 (1980).
[16] R. E. Kidder, Nucl. Fusion **8**, 3 (1968); B. J. Gitomer, R. L. Morse, and B. S. Newberger, Phys. Fluids **20**, 234 (1977); C. E. Max, C. F. Mackee, and W. C. Mead, Phys. Fluids **23**, 234 (1980); P. Mora, Phys. Fluids **25**, 1051 (1982).
[17] M. H. Key, W. T. Toner, T. J. Goldsack, J. D. Kilkenny, S. A. Veats, P. F. Cunningham, and C. L. S. Lewis, Phys. Fluids **26**, 2011 (1983); T. Boehly, K. A. Tanaka, T. Mochizuki, and C. Yamanaka, J. Appl. Phys. **60**, 3840 (1986).
[18] T. Yuchi and K. Nishihara, Technol. Rep. Osaka Univ. **32**, 295 (1982); G. B. Zimmerman and R. M. More, J. Quant. Spectrosc. Radiat. Transfer **23**, 517 (1980); R. M. More, J. Quant. Spectrosc. Radiat. Transfer **27**, 345 (1982); S. Atzeni, A. Caruso, and V. A. Pais, Laser Part. Beams **4**, 393 (1986).